

Classifying Topological Charge in SU(3) Yang-Mills Theory with Machine Learning

Takuya Matsumoto¹, Masakiyo Kitazawa^{†1,2}, and Yasuhiro Kohno³

¹*Department of Physics, Osaka University, Toyonaka, Osaka 560-0043, Japan*

²*J-PARC Branch, KEK Theory Center, Institute of Particle and Nuclear Studies, KEK, 203-1, Shirakata, Tokai, Ibaraki, 319-1106, Japan*

³*Research Center for Nuclear Physics, Osaka University, Ibaraki, Osaka 567-0047, Japan*

.....
 We apply a machine learning technique for identifying the topological charge of quantum gauge configurations in four-dimensional SU(3) Yang-Mills theory. The topological charge density measured on the original and smoothed gauge configurations with and without dimensional reduction is used as inputs for the neural networks (NN) with and without convolutional layers. The gradient flow is used for the smoothing of the gauge field. We find that the topological charge determined at a large flow time can be predicted with high accuracy from the data at small flow times by the trained NN; for example, the accuracy exceeds 99% with the data at $t/a^2 \leq 0.3$. High robustness against the change of simulation parameters is also confirmed with a fixed physical volume. We find that the best performance is obtained when the spatial coordinates of the topological charge density are fully integrated out in preprocessing, which implies that our convolutional NN does not find characteristic structures in multi-dimensional space relevant for the determination of the topological charge.

[†] kitazawa@phys.sci.osaka-u.ac.jp

1 Introduction

Quantum chromodynamics (QCD) and other Yang-Mills gauge theories in four space-time dimensions can have topologically non-trivial gauge configurations classified by the topological charge \mathcal{Q} taking integer values. The existence of non-trivial topology in QCD is responsible for various non-perturbative aspects of this theory, such as the U(1) problem [1]. The susceptibility of \mathcal{Q} also provides an essential parameter relevant to the cosmic abundance of the axion dark matter [2–4].

The topological property of QCD and Yang-Mills theories has been studied by numerical simulations of lattice gauge theory [5–18]. Because of the discretization of spacetime, gauge configurations on the lattice are, strictly speaking, topologically trivial. However, it is known that well-separated topological sectors emerge when the continuum limit is approached [19]. Various methods for the measurement of \mathcal{Q} for gauge configurations on the lattice have been proposed, which are roughly classified into the fermionic and gluonic ones. In the fermionic definitions the topological charge is defined through the Atiyah-Singer index theorem [20], while the gluonic definitions make use of the topological charge measured on a smoothed gauge field [21, 22]. The values of \mathcal{Q} measured by various methods show approximate agreement [14], which indicates the existence of well-separated topological sectors. In lattice simulations, the measurement of the topological charge is also important for monitoring topological freezing [23–26].

In the present study, we apply the machine learning (ML) techniques for analyzing \mathcal{Q} for gauge configurations on the lattice. The ML has been applied for various problems in computer science quite successfully, such as the image recognition, object detection, and natural language processing [27–44]. Recently, this technique has also been applied to problems in physics [45–60]. In the present study, we generate data by the numerical simulation of SU(3) Yang-Mills theory in four spacetime dimensions, and feed them into the neural networks (NN). The NN are trained to predict the value of \mathcal{Q} by the supervised learning. We use the convolutional NN (CNN) as well as the simple fully-connected NN (FNN) depending on the type of the input data.

The first aim of this study is development of an efficient algorithm for the analysis of \mathcal{Q} with the aid of the ML. The second, and more interesting, purpose is the search for characteristic local structures in the four-dimensional space related to \mathcal{Q} by the CNN. The CNN is a class of NN that was developed for image recognition [28, 31–33]. The CNN has so-called convolutional layers which are composed of filters analyzing a small spatial region of the output of the previous layer. If features of the data related to the answer are embedded in the filter window, the convolutional layers can be trained to output a signal related to these

features. This design of the CNN had turned out to be quite effective in image recognition, i.e. the analysis of two-dimensional data [28, 31–33]. It is thus expected that the CNN is also suitable for the analysis of four-dimensional data. It is known that Yang-Mills theories have classical gauge configurations called instantons, which carry a nonzero topological charge and have a localized structure [1]. If the topological charge of the quantum gauge configurations is also carried by instanton-like local objects in four-dimensional space, a four-dimensional CNN would recognize and make use of them for the prediction of \mathcal{Q} . Such an analysis of four-dimensional quantum fields by ML will open up a new application of this technique.

In this study, we use the topological charge density measured on the original and smoothed gauge configurations as inputs to the NN. The smoothing is performed by the gradient flow [61–63]. We also try dimensional reduction to various dimensions as preprocessing of the data before feeding them into a CNN or FNN. For the definition of \mathcal{Q} , we use a gluonic one through the gradient flow [62, 63]. We find that the NN can estimate the value of \mathcal{Q} determined at a large flow time with high accuracy from the data obtained at small flow times. In particular, we show that a high accuracy is obtained by multi-channel analysis of the data at different flow times. We argue that this method can be used for the analysis of \mathcal{Q} in SU(3) Yang-Mills theory with a reduction in numerical cost.

To evaluate the performance of the NN searching for high-dimensional data, we compare the resulting accuracies obtained with and without the dimensional reduction. From this comparison we find that the accuracy does not have a statistically significant dependence on the dimension of the input data. This result implies that the CNN fails in finding characteristic features related to the topology in multi-dimensional space, i.e. the quantum gauge configurations do not have such features, or their signals are too complicated or too weak to be detected by the CNN.

2 Organization of this paper

In this study, we perform various analyses of the topological charge \mathcal{Q} by CNN or FNN. One of them is the analysis of the topological charge density $q_t(x)$ in the four-dimensional ($d = 4$) space at a flow time t (the definitions of $q_t(x)$ and t will be given in Sec. 4). We also perform the dimensional reduction of the input data as preprocessing and analyze them using the NN. The dimension of the data is reduced to $d = 0 - 3$ by integrating out spatial coordinates. For the analysis at $d = 0$ we adopt an FNN, while the data at $d \geq 1$ are analyzed by a CNN. We then compare the accuracy of the trained NN obtained for each input dimension. If features in the four-dimensional space are too abstract to be recognized by the NN, the dimensional reduction will improve the accuracy of the trained NN. On the other

β	N^4	N_{conf}
6.2	16^4	20,000
6.5	24^4	20,000

Table 1 Simulation parameters on the lattice: the inverse bare coupling β , the lattice size N^4 , and the number of configurations N_{conf} .

hand, if characteristic features are lost by the dimensional reduction, this procedure would lower the accuracy.

In the present study we find that the resulting accuracy of the NN is insensitive to the value of d . Because the numerical cost for the supervised learning is suppressed as d becomes smaller, this means that the analysis of the $d = 0$ data is most efficient. In this paper, therefore, we first report this most successful result among various analyses with the ML technique in Sec. 6. The analyses of the multi-dimensional data will then be discussed later in Secs. 7 and 8.

Before introducing the ML technique, we consider simple models to make an estimate of \mathcal{Q} without ML in Sec. 5. These models are used for benchmarks of the trained NN in Secs. 6–8.

The whole structure of this paper is summarized as follows. In the next section, we describe the setup of the lattice numerical simulations. In Sec. 4, we give a brief review of the analysis of the topology with the gradient flow. The benchmark models for the classification of \mathcal{Q} without using ML are discussed in Sec. 5. The application of ML is then discussed in Secs. 6–8. We first consider the analysis of the $d = 0$ data by FNN in Sec. 6. We discuss the analysis of the four-dimensional field $q_t(x)$ by CNN in Sec. 7. In Sec. 8, we extend the analysis to $d = 1, 2, 3$. The last section is devoted to discussions.

3 Lattice setup

Throughout this paper, we consider SU(3) Yang-Mills theory in four-dimensional Euclidean space with periodic boundary conditions for all directions. The standard Wilson gauge action is used for generating the gauge configurations. We perform the numerical analyses at two inverse bare couplings $\beta = 6/g^2 = 6.2$ and 6.5 with lattice volumes 16^4 and 24^4 , respectively, as shown in Table 1. These lattice parameters are chosen so that the lattice volumes in physical units L^4 are almost the same on these lattices; the lattice spacing determined in Ref. [18] shows that the difference in the lattice size L is less than 2%. The

lattice size L is related to the critical temperature of the deconfinement phase transition T_c as $1/L \simeq 0.63T_c$ [64].

We generate 20,000 gauge configurations for each β , which are separated by 100 Monte Carlo sweeps from each other, where one sweep consists of one pseudo-heat bath and five over-relaxation updates. For the discretized definition of the topological charge density on the lattice, we use the operator constructed from the clover representation of the field strength. The gradient flow is used for the smoothing of the gauge field.

To estimate the statistical error of an observable on the lattice, we use jackknife analysis with the binsize 100. We have numerically checked that the auto-correlation length of the topological charge is about 100 and 1900 sweeps for $\beta = 6.2$ and 6.5, respectively. The binsize of the jackknife analysis including 100×100 sweeps is sufficiently larger than the auto-correlation length.

4 Topological charge

In the continuous Yang-Mills theory in four-dimensional Euclidean space, the topological charge is defined by

$$\mathcal{Q} = \int_V d^4x q(x), \quad (1)$$

$$q(x) = -\frac{1}{32\pi^2} \epsilon_{\mu\nu\rho\sigma} \text{tr} [F_{\mu\nu}(x) F_{\rho\sigma}(x)], \quad (2)$$

where V is the four-volume and $F_{\mu\nu}(x) = \partial_\mu A_\nu(x) - \partial_\nu A_\mu(x) + [A_\mu(x), A_\nu(x)]$ is the field strength. $q(x)$ is called the topological-charge density with the coordinate x in Euclidean space.

In lattice gauge theory, Eq. (1) calculated on a gauge configuration with a discretized definition of Eq. (2) is not given by an integer, but distributes continuously. To obtain discretized values, one may apply a smoothing of the gauge field before the measurement of $q(x)$.

In the present study, we use the gradient flow [62, 63] for the smoothing. The gradient flow is a continuous transformation of the gauge field characterized by a parameter t called the flow time having dimension of mass inverse squared. The gauge field at a flow time t is a smoothed field with the mean-square smoothing radius $\sqrt{8t}$ [62]. In the following, we denote the topological charge density obtained at t as $q_t(x)$, and its four-dimensional integral as

$$Q(t) = \int_V d^4x q_t(x). \quad (3)$$

Shown in Fig. 1 is the t dependence of $Q(t)$ calculated on 200 gauge configurations at $\beta = 6.2$ and 6.5. The horizontal axis shows the dimensionless flow time t/a^2 with the lattice

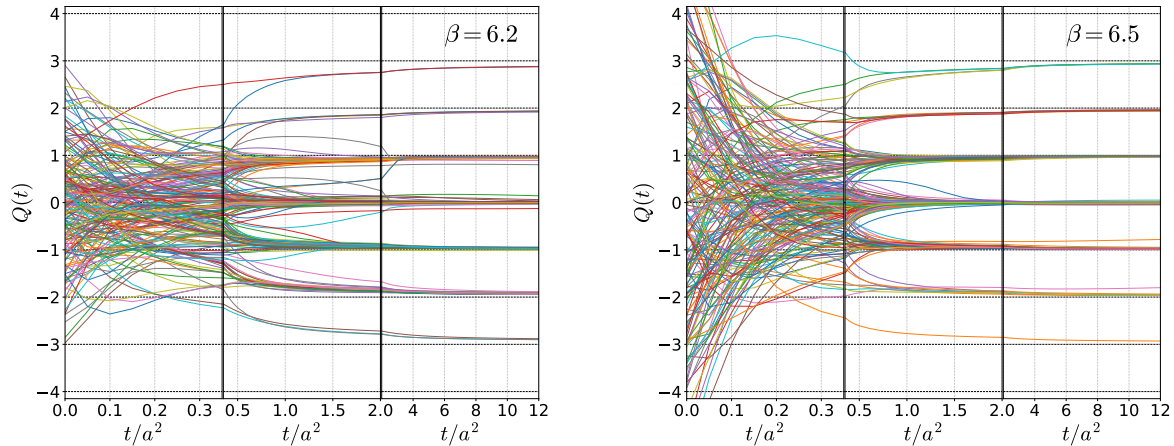


Fig. 1 Flow time t dependence of $Q(t)$ on 200 gauge configurations at $\beta = 6.2$ (left) and 6.5 (right). The range of the flow time t is divided into three panels representing $0 \leq t/a^2 \leq 0.35$, $0.35 \leq t/a^2 \leq 2$, and $2 \leq t/a^2 \leq 12$.

spacing a . One finds that the values of $Q(t)$ approach discrete integer values as t becomes larger. In Fig. 2, we show the distribution of $Q(t)$ for several values of t/a^2 by the histogram at $\beta = 6.5$. At $t = 0$, the values of $Q(t)$ are distributed continuously around the origin. As t becomes larger, the distribution converges on discretized integer values. For $t/a^2 > 1.0$, the distribution is almost completely separated around integer values. In this range of t , one can classify the gauge configurations into different topological sectors labeled by the integer topological charge \mathcal{Q} defined, for example, by the nearest integer to $Q(t)$. It is known that the value of \mathcal{Q} defined in this way approximately agrees with the topological charge obtained through other definitions, and the agreement is better on finer lattices [14].

From Figs. 1 and 2, one finds that the distribution of $Q(t)$ deviates from integer values toward the origin. This deviation becomes smaller as t becomes larger. From Fig. 1, one also finds that $Q(t)$ on some gauge configurations has a “flipping” between different topological sectors; after $Q(t)$ shows a convergence to an integer value, it sometimes jumps into another integer [14]. As this behavior decreases on the finer lattice, the flipping would be regarded as a lattice artifact arising from the ambiguity of the topological sectors on the discretized spacetime.

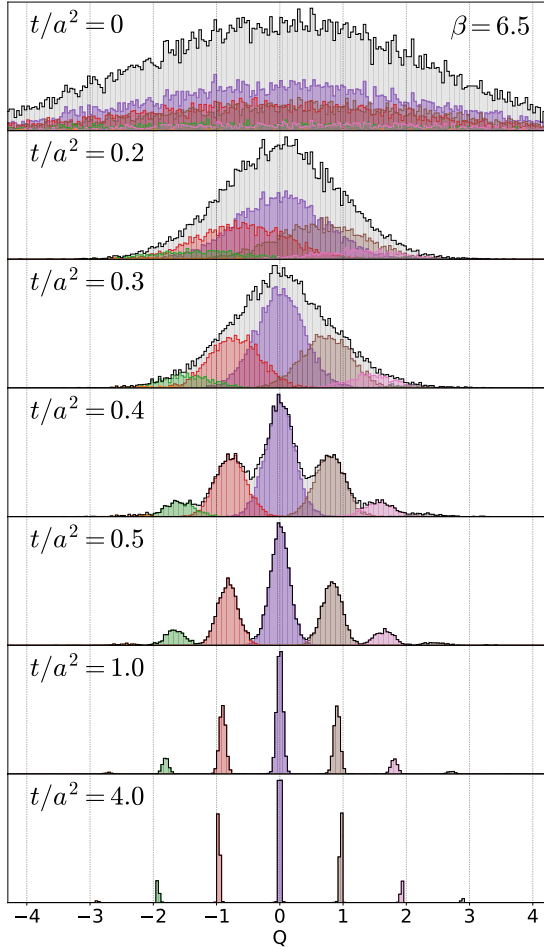


Fig. 2 Distribution of $Q(t)$ at several values of t/a^2 . The colored histograms are the distributions in individual topological sectors; see text.

Q	-5	-4	-3	-2	-1	0	1	2	3	4	5	$\langle Q^2 \rangle$
$\beta = 6.2$	2	17	235	1325	4571	7474	4766	1352	240	18	0	1.247(15)
$\beta = 6.5$	0	5	105	1080	4639	8296	4621	1039	202	13	0	1.039(47)

Table 2 Number of the gauge configurations classified into each topological sector with the definition of Q in Eq. (4). The far right column shows the variance of the distribution of Q .

In the following, for the numerical definition of the topological charge Q of each gauge configuration we employ

$$\text{round}[Q(t)]_{t/a^2=4.0}, \quad (4)$$

where $\text{round}(x)$ means rounding off to the nearest integer. As indicated from Fig. 1, the value of \mathcal{Q} hardly changes with the variation of t/a^2 in the range $4 < t/a^2 < 12$. In Table 2, we show the number of gauge configurations classified into each topological sector through this definition. The variance of this distribution $\langle \mathcal{Q}^2 \rangle$ is shown in the far right column. In Fig. 2, the distributions of $Q(t)$ in individual topological sectors are shown by the colored histograms.

5 Benchmark models

In this study, we analyze $q_t(x)$ or $Q(t)$ at small values of t by the ML technique. Here, t used for the input has to be chosen small enough that a simple estimate of \mathcal{Q} like Eq. (4) is not possible. In this section, before the main analysis with the ML technique we discuss the accuracy obtained only from $Q(t)$ without ML. These analyses serve as benchmarks for evaluating the genuine benefit of ML.

Throughout this study, as the performance metric of a model for an estimate of \mathcal{Q} we use the accuracy defined by

$$P = \frac{\text{number of correct answers}}{\text{number of total data}}. \quad (5)$$

Because the numbers of gauge configurations on different topological sectors differ significantly as in Table 2, Eq. (5) would not necessarily be a good performance metric. In particular, the topological sector with $\mathcal{Q} = 0$ has the largest number, and a model which estimates $\mathcal{Q} = 0$ for all configurations obtains the accuracy $P \simeq 0.37$ (0.41) for $\beta = 6.2$ (6.5), although such a model is, of course, meaningless. One has to keep in mind this possible problem of Eq. (5). In Secs. 6 and 7, we use the recalls of individual topological sectors $R_{\mathcal{Q}}$ defined by

$$R_{\mathcal{Q}} = \frac{N_{\mathcal{Q}}^{\text{correct}}}{N_{\mathcal{Q}}}, \quad (6)$$

complementary to Eq. (5) to inspect the bias of NN models, where $N_{\mathcal{Q}}$ is the number of configurations in the topological sector \mathcal{Q} and $N_{\mathcal{Q}}^{\text{correct}}$ is the number of correct answers among them.

To make an estimate of \mathcal{Q} from $Q(t)$, we consider two simple models. The first model is just rounding off $Q(t)$ as

$$Q_{\text{naive}} = \text{round}[Q(t)]. \quad (7)$$

The accuracy obtained by this model, P_{naive} , as a function of t is shown in Fig. 3 by the dashed lines. The figure shows that the accuracy of Eq. (7) approaches 100% as t/a^2 becomes larger

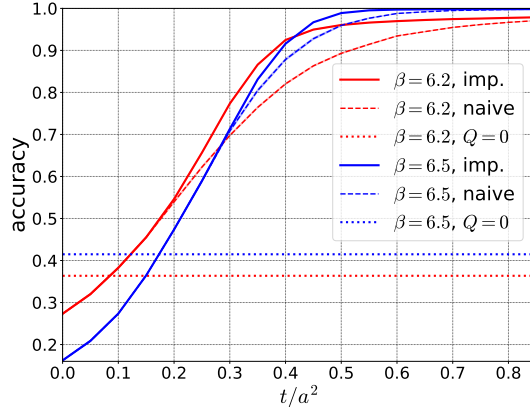


Fig. 3 Flow time t dependence of the accuracies P_{naive} and P_{imp} obtained by the models Eqs. (7) and (8), respectively. The dotted lines show the accuracy of the model that answers $Q = 0$ for all configurations.

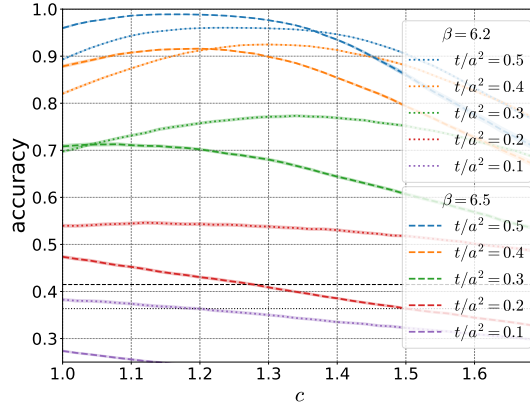


Fig. 4 Accuracy of Eq. (8) as a function of c for several values of t/a^2 . The statistical errors are shown by the shaded band, although the width of the bands are almost the same as the thickness of the lines.

corresponding to the behavior of $Q(t)$ in Figs. 1 and 2. At $t/a^2 = 4.0$, Eq. (7) is equivalent to Eq. (4) and the accuracy becomes 100% by definition.

The model in Eq. (7) can be improved with a simple modification. In Fig. 2, one sees that the distribution in each topological sector is shifted toward the origin from Q . This behavior

t/a^2	$\beta = 6.2$	$\beta = 6.5$
0	0.273(3)	0.162(3)
0.1	0.383(4)	0.274(3)
0.2	0.546(4)	0.474(4)
0.3	0.773(3)	0.713(4)
0.4	0.925(2)	0.916(2)
0.5	0.960(1)	0.989(1)
1.0	0.982(1)	0.999(0)
2.0	0.992(1)	0.999(0)
4.0	1.000(0)	1.000(0)
10.0	0.993(1)	0.999(0)

Table 3 Accuracy P_{imp} obtained by the model Eq. (8) with the optimization of c .

suggests that Eq. (7) can be improved by applying a constant before rounding off,

$$Q_{\text{imp}} = \text{round}[cQ(t)], \quad (8)$$

where c is a parameter determined so as to maximize the accuracy in the range $c > 1$ for each t . In Fig. 4, we show the c dependence of the accuracy of Eq. (8) for several values of t/a^2 . The figure shows that the accuracy has a maximum at $c > 1$ for some t/a^2 . In this case, the model Eq. (8) has a better accuracy than Eq. (7) by tuning the parameter c . We denote the optimal accuracy of Eq. (8) as P_{imp} . In Fig. 3, the t/a^2 dependence of P_{imp} is shown by the solid lines. The numerical values of P_{imp} are depicted in Table 3 for some t/a^2 . Figure 3 shows that a clear improvement of the accuracy by the single-parameter tuning is observed at $t/a^2 \gtrsim 0.2$ and 0.3 for $\beta = 6.2$ and 6.5 , respectively. We note that $P_{\text{naive}} = P_{\text{imp}} = 1$ at $t/a^2 = 4.0$ by definition. Table 3 also shows that P_{imp} is almost unity at $t/a^2 = 2.0$ and 10.0 , which shows that the value of Q defined by Eq. (4) hardly changes with the variation of t/a^2 in the range $t/a^2 \gtrsim 2.0$.

As P_{imp} is already close to unity at $t/a^2 = 0.5$, it is difficult to obtain a non-trivial gain in the accuracy from the analysis of $q_t(x)$ by NN for $t/a^2 \geq 0.5$. In the following, therefore, we feed the data at $t/a^2 < 0.5$ to the NN. In the following sections, we use P_{imp} for a benchmark of the accuracy obtained by the NN models.

layer	output size	activation
input	3	-
full connect	5	logistic
full connect	1	-

Table 4 Design of the FNN used for the analysis of $Q(t)$.

6 Learning $Q(t)$

From this section we employ the ML technique for the analysis of the lattice data. As discussed in Secs. 1 and 2, among various analyses we found that the most efficient result is obtained when a set of the values of $Q(t)$ at several t is analyzed by FNN. In this section, we discuss this result. The analysis of the multi-dimensional data by CNN will be reported in later sections.

6.1 Setting

In this section we employ a simple FNN model without convolutional layers. The FNN accepts three values of $Q(t)$ at different t as inputs, and is trained to predict \mathcal{Q} by supervised learning. The structure of the FNN is shown in Table 4. The FNN has only one hidden layer with five units that are fully connected with the input and output layers. We use the logistic (sigmoid) function for the activation function of the hidden layer. Although we have also tried the rectified linear unit (ReLU) for the activation function, we found that the logistic function gives a better result. We employ the regression model, i.e. the output of the FNN is given by a single real number. The final prediction of \mathcal{Q} is then obtained by rounding off the output to the nearest integer.

For the supervised learning, we randomly divide 20,000 gauge configurations into 10,000 and two 5,000 sub-groups. We use 10,000 data for the training, and one of the 5,000 data sets for the validation analysis. The last 5,000 data are used for the evaluation of the accuracy of the trained NN. The supervised learning is repeated 10 times with different divisions of the configurations, and the uncertainty of the accuracy is estimated from the variance¹.

We use the mean-squared error for the loss function, and minimize it through the updates of the NN parameters by the ADAM [65] with the default setting. The update is repeated for

¹ This analysis is called the shuffle-split cross validation. There are alternative evaluations of the stability, such as the k -fold cross validation. As the resulting error would not be changed so much, however, we only use the shuffle-split cross validation throughout this study.

input t/a^2	$\beta = 6.2$	$\beta = 6.5$
0.45, 0.4, 0.35	0.974(2)	0.998(1)
0.4, 0.35, 0.3	0.975(2)	0.997(1)
0.35, 0.3, 0.25	0.967(2)	0.996(1)
0.3, 0.25, 0.2	0.959(2)	0.990(2)
0.25, 0.2, 0.15	0.939(3)	0.951(2)
0.2, 0.15, 0.1	0.864(3)	0.831(5)
0.15, 0.1, 0.05	0.692(4)	0.647(8)
0.1, 0.05, 0	0.538(5)	0.499(6)
0.4, 0.3, 0.2	0.971(2)	0.995(1)
0.3, 0.2, 0.1	0.941(2)	0.957(2)
0.2, 0.1, 0	0.741(3)	0.682(4)

Table 5 Accuracy of the trained FNN in Table 4 with various sets of the input data. Left column shows the values of t/a^2 that evaluate $Q(t)$ for the input. Errors are estimated from the variance among 10 different trainings.

3,000 epochs with batchsize 16. The optimized parameter set of the FNN is then determined as the one giving the lowest value of the loss function on the validation data.

The FNN is implemented by the Chainer framework [66]. The training of the FNN in this section has been carried out as a single-core job on a XEON processor (Xeon E5-2698-v3). It takes about 40 minutes for a single training in this environment.

6.2 Result

Shown in Table 5 are the accuracies obtained by the trained FNN for various choices of the input data. The left column shows the set of three flow times t/a^2 that evaluate $Q(t)$ used for the input of the FNN. In the upper eight rows we show the results with the input flow times $t/a^2 = (\hat{t}_{\max}, \hat{t}_{\max} - 0.05, \hat{t}_{\max} - 0.1)$. The table shows that the accuracy is improved as \hat{t}_{\max} becomes larger. By comparing this result with Table 3 one finds that the accuracy obtained by the FNN is significantly higher than P_{imp} at $t/a^2 = \hat{t}_{\max}$. In particular, the accuracy at $\hat{t}_{\max} = 0.3$, i.e. $t/a^2 = (0.3, 0.25, 0.2)$, shown in bold is as high as 99% for $\beta = 6.5$, while the benchmark model Eq. (8) gives $P_{\text{imp}} \simeq 0.71$. This result shows that the prediction of \mathcal{Q} from the numerical data at $t/a^2 \leq 0.3$ is remarkably improved with the aid of the ML technique. Table 5 also shows that the accuracy improves further as \hat{t}_{\max} becomes larger, but the improvement from P_{imp} is limited for much larger \hat{t}_{\max} because P_{imp} is already

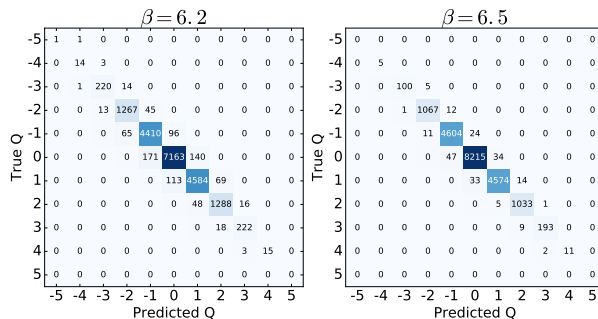


Fig. 5 Confusion matrix of the trained FNN model with the input $Q(t)$ at $t/a^2 = (0.3, 0.25, 0.2)$ for $\beta = 6.2$ (left) and 6.5 (right). Each cell shows the number of configurations with the true and predicted values of Q .

β	P	R_Q									
		-4	-3	-2	-1	0	1	2	3	4	
6.2	0.959	0.912	0.933	0.953	0.964	0.959	0.964	0.947	0.919	0.949	
6.5	0.990	1.000	0.951	0.987	0.993	0.991	0.988	0.992	0.946	0.818	

Table 6 Accuracy P and the recalls of individual topological sectors R_Q obtained by the FNN with the input $Q(t)$ at $t/a^2 = (0.3, 0.25, 0.2)$.

close to unity. The same tendency is obtained for $\beta = 6.2$, although the accuracy is slightly lower than $\beta = 6.5$.

In Fig. 5 we show the confusion matrix that plots the numbers of configurations with the true and predicted values of Q with the input flow times $t/a^2 = (0.3, 0.25, 0.2)$ for $\beta = 6.2$ and 6.5 . From the figure one finds that the deviation of the output of the FNN from the true value is at most ± 1 . In Table 6, the recalls from Eq. (6) of individual topological sectors are shown. The table shows that R_Q tends to be suppressed as $|Q|$ becomes larger, but its Q dependence is mild. This result suggests that the training of the FNN is successful in spite of the biased Q distribution of the training data. See also the analysis in Sec. 6.4.

The high accuracy obtained in this analysis is not surprising qualitatively. As shown in Fig. 1, for many configurations the behavior of $Q(t)$ is monotonic at $0.2 \leq t/a^2 \leq 0.3$. Therefore, the value at large t can be estimated easily, for example, by the human eye, for almost all configurations. It is reasonable to interpret that the FNN learns this behavior.

We, however, remark that the accuracy of 99% obtained by the trained FNN is still non-trivial. We have tried to find a simple function to predict \mathcal{Q} from three values of $Q(t)$ at $t/a^2 = (0.3, 0.25, 0.2)$, and also performed blind tests with human beings. These trials have been able to obtain 95% accuracy easily, but have failed in attaining 99%; see Appendix A for more discussion on this point. These results suggest that ML finds non-trivial features in the behavior of $Q(t)$.

In the lower three rows of Table 5, we show the accuracies of the trained FNN with the input flow times $t/a^2 = (\hat{t}_{\max}, \hat{t}_{\max} - 0.1, \hat{t}_{\max} - 0.2)$ for several values of \hat{t}_{\max} . These accuracies are slightly lower than the results with $t/a^2 = (\hat{t}_{\max}, \hat{t}_{\max} - 0.05, \hat{t}_{\max} - 0.1)$ at the same \hat{t}_{\max} . We have also tested the FNN models analyzing four values of $Q(t)$. It, however, was found that the accuracy does not exceed the case with three input data with the same maximum t/a^2 . We have also tested FNN models with more complex structure, for example, with multiple hidden layers. A statistically significant improvement of the accuracy, however, was not observed here either.

In the conventional analysis of \mathcal{Q} with the gradient flow discussed in Sec. 4, one uses the value of $Q(t)$ at a large flow time at which the distribution of $Q(t)$ is well localized. This means that the gradient flow equation has to be solved numerically [62] up to the large flow time. Moreover, concerning the continuum $a \rightarrow 0$ limit it is suggested that the flow time has to be fixed in physical units [18], which means that the flow time in lattice units, t/a^2 , becomes large as the continuum limit is approached. On the other hand, our analysis with the aid of the FNN can estimate \mathcal{Q} successfully only with the data at $t/a^2 \lesssim 0.3$, and thus the numerical cost for solving the gradient flow can be reduced².

Table 5 shows that better accuracy is obtained on the finer lattice (larger β). From Fig. 1, it is suggested that this tendency comes from the reduction of the “flipping” of $Q(t)$ on the finer lattice, as the non-monotonic flipping makes the prediction of \mathcal{Q} from $Q(t)$ at small t/a^2 difficult. This effect is also suggested from Fig. 3, as P_{naive} and P_{imp} at $\beta = 6.2$ are lower than those at $\beta = 6.5$. We note that this lattice spacing dependence hardly changes even if

²In Yang-Mills theories this cost reduction is practically beneficial. The most numerically demanding part in typical Yang-Mills lattice simulations except for the gradient flow is the gauge updates, because the cost for the measurement of gauge observables is usually negligible. The numerical costs of the gauge updates and the gradient flow are dominated by the calculation of staples. From the numbers to calculate staples in both algorithms one finds that the cost for the gradient flow up to $t/a^2 \simeq 4.0$ corresponds to the gauge updates of $\mathcal{O}(100)$ sweeps. In Yang-Mills theories measurements of gauge observables are usually performed with much shorter Monte-Carlo separations, $\lesssim \mathcal{O}(10)$, because it is responsible for the noise reduction. This is true even when the auto-correlation length of \mathcal{Q} is large, because statistical fluctuation of gauge observables are typically significantly larger than the \mathcal{Q} dependence of the observables. To realize such frequent measurements, the cost reduction for the measurement of \mathcal{Q} from $\mathcal{O}(100)$ sweeps is highly desirable.

we scale the value of t to determine \mathcal{Q} in Eq. (4) in physical units if t is sufficiently large. Provided that the flipping of $Q(t)$ comes from the lattice artifact related to the ambiguity of the topological sectors on the discretized spacetime, it is conjectured that the imperfect accuracy of the FNN is to a large extent attributed to this lattice artifact. Then, the imperfect accuracy of the FNN at finite a is inevitable, and the accuracy should become better as the lattice spacing becomes finer. Therefore, it is conjectured that the systematic uncertainty arising from the imperfect accuracy of the FNN is suppressed in the analysis of the continuum extrapolation.

6.3 Susceptibility and higher-order cumulants

Next, we consider the variance of the topological charge, $\langle \mathcal{Q}^2 \rangle$, which is related to the topological susceptibility as $\chi_Q = \langle \mathcal{Q}^2 \rangle / V$. From the output of the FNN with the input flow times $t/a^2 = (0.3, 0.25, 0.2)$, the variance of \mathcal{Q} is calculated to be

$$\langle \mathcal{Q}^2 \rangle_{\text{NN}} = 1.253(15)(2) \quad (\text{for } \beta = 6.2), \quad (9)$$

$$\langle \mathcal{Q}^2 \rangle_{\text{NN}} = 1.037(46)(1) \quad (\text{for } \beta = 6.5), \quad (10)$$

where the first and second errors represent the statistical error obtained by the jackknife analysis and the uncertainty of the FNN model estimated from 10 different trainings, respectively. These values agree well with those shown in Table 2.

From the output of the FNN the fourth- and sixth-order cumulants of \mathcal{Q} are calculated to be $\langle \mathcal{Q}^4 \rangle_{c,\text{NN}} = 0.30(6)(0)$ and $\langle \mathcal{Q}^6 \rangle_{c,\text{NN}} = -1.16(41)(12)$ for $\beta = 6.2$, and $\langle \mathcal{Q}^4 \rangle_{c,\text{NN}} = 0.35(11)(1)$ and $\langle \mathcal{Q}^6 \rangle_{c,\text{NN}} = -0.82(46)(1)$ for $\beta = 6.5$. On the other hand, the cumulants extracted from the distribution in Table 2 are $\langle \mathcal{Q}^4 \rangle_c = 0.38(7)$ and $\langle \mathcal{Q}^6 \rangle_c = -1.11(49)$ for $\beta = 6.2$, and $\langle \mathcal{Q}^4 \rangle_c = 0.39(12)$ and $\langle \mathcal{Q}^6 \rangle_c = -0.82(52)$ for $\beta = 6.5$. One thus finds that the values of $\langle \mathcal{Q}^4 \rangle_c$ and $\langle \mathcal{Q}^6 \rangle_c$ estimated by the FNN are consistent with the original values within the statistics. These results, of course, do not mean that the FNN can make a prediction for arbitrary higher-order cumulants. In fact, Fig. 5 suggests that the accuracy becomes worse for large $|\mathcal{Q}|$. This behavior would modify higher-order cumulants more strongly. We also note that these results are obtained only with specific setups of the lattice simulation. There are no guarantees of obtaining a similar stability when the setup, for example, the lattice volume and gauge action, is changed. It, however, is worth emphasizing that the FNN developed in this study can reproduce even the sixth-order cumulant within the statistics for at least two simulation setups.

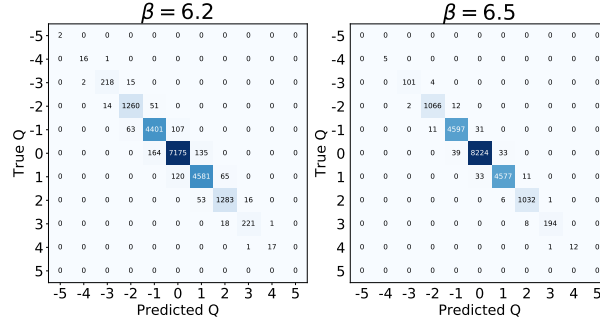


Fig. 6 Confusion matrix of the FNN model trained only with the training data at $|\mathcal{Q}| \leq 3$. The input flow times are $t/a^2 = (0.3, 0.25, 0.2)$.

6.4 Training with restricted data sets

As shown in Table 2, the probability of the appearance of large $|\mathcal{Q}|$ is severely suppressed. Therefore, it is practically possible that the FNN encounters a large $|\mathcal{Q}|$ that the FNN has never experienced during the training phase. In this subsection, we study the response of the FNN for \mathcal{Q} that is not included in the training data.

For this purpose, we prepare training and validation data sets composed only of $|\mathcal{Q}| \leq 3$. We then perform the supervised learning of the FNN using these restricted data sets. The input flow times are $t/a^2 = (0.3, 0.25, 0.2)$. The setup of the supervised learning is the same as before except for the restriction of the training data.

In Fig. 6, we show examples of the confusion matrix of the FNN models trained by the data with $|\mathcal{Q}| \leq 3$ for $\beta = 6.2$ and 6.5 . The total accuracy of the FNN is $P = 0.959$ and 0.990 for $\beta = 6.2$ and 6.5 , respectively, which are consistent with the training without the restriction. From Fig. 6 one finds that the trained FNN can predict a correct answer even for large $|\mathcal{Q}|$ that are not included in the training data. Moreover, comparison with Fig. 5 shows that the accuracies for the topological sectors $|\mathcal{Q}| = 4$ and 5 hardly change with and without the restriction.

This result is not surprising. First, we employ a regression model for the FNN, i.e. the output of the FNN is given by a single number, rather than a classification model that outputs probabilities of predetermined categories. Therefore, the answers of the FNN are not restricted to specific values. Second, from the behaviors of $Q(t)$ in Fig. 1 this result is also expected as $Q(t)$ in different topological sectors behaves differently around $0.2 \leq t/a^2 \leq 0.3$. Finally, as in Table 2 the number of configurations with $|\mathcal{Q}| = 4$ and 5 are small in the data set; 0.18% and 0.09% for $\beta = 6.2$ and 6.5 , respectively. Their effects on the supervised learning thus should be small even if they are included in the training data.

N_{train}	10,000	5,000	1,000	500	100
$\beta = 6.2$	0.959(2)	0.959(2)	0.959(2)	0.953(3)	0.903(7)
$\beta = 6.5$	0.990(2)	0.990(2)	0.989(2)	0.989(1)	0.902(8)

Table 7 Dependence of the accuracy of the trained FNN on the number of the training data N_{train} .

		analyzed data	
		$\beta = 6.2$	$\beta = 6.5$
training data	$\beta = 6.2$	0.959(2)	0.986(2)
	$\beta = 6.5$	0.956(2)	0.990(2)
	6.2/6.5	0.958(1)	0.989(2)

Table 8 Accuracy obtained by the analysis of the data with different β from the one used for the training. Last row shows the accuracy of the FNN trained by the mixed data set at $\beta = 6.2$ and 6.5 .

We, however, stress that this result does not mean that the trained FNN can make a prediction for arbitrarily large $|\mathcal{Q}|$ successfully. As the result in this subsection is obtained only for particular data sets, in general one has to be careful when applying NN for the analysis of the data that are not included in the training data.

6.5 Reduction of training data

So far, we have performed the training of the FNN with the number of training data points $N_{\text{train}} = 10,000$. Now we consider training with much smaller N_{train} .

Shown in Table 7 is the accuracy of the trained FNN with various N_{train} with the input flow times $t/a^2 = (0.3, 0.25, 0.2)$. The structure of the FNN is the same as before. From the table, one finds that the FNN is successfully trained even with $N_{\text{train}} = 500$.

This result shows that the cost for the preparation of the training data can be reduced. The reduction of N_{train} is also responsible for reducing the numerical cost for the training. With $N_{\text{train}} = 10,000$, the training of the FNN requires about 40 minutes on a single core of a XEON processor, while only 5.5 minutes is needed with $N_{\text{train}} = 500$ on the same environment.

6.6 Robustness

Next, we consider an application of the FNN for the analysis of data obtained at different β from the one used for the training. In Table 8, we show the accuracy obtained with various combinations of the β values used for training and analysis with the input flow times $t/a^2 = (0.3, 0.25, 0.2)$. The table shows that the accuracy becomes worse when the different data set is analyzed, but the reduction is small and almost within the statistics. We have also performed the training of the FNN with a combined data set of $\beta = 6.2$ and 6.5 . The result of this analysis is shown in the far bottom row in Table 8. One finds that this FNN can predict Q for each β with the same accuracy within the statistics as those trained for individual β .

From these results it is conjectured that a NN trained by the combined data sets at $\beta = 6.2$ and 6.5 can analyze the gauge configurations in the parameter range $6.2 \leq \beta \leq 6.5$ obtained by the Wilson gauge action with a high accuracy. Moreover, the range of β would be extended by performing the supervised learning with the data at different β values. Once such a model is developed, it can be used for the analysis of various β values and will play a useful role.

The two lattices studied here have almost the same spatial volume in physical units. Therefore, in the present study the robustness against variation of the spatial volume in physical units is not studied. To check the volume dependence, one has to generate gauge configurations with different spatial volumes and repeat the same analysis. This analysis is left for future work.

Because the analysis in the present study is performed only for SU(3) gauge theory with the Wilson gauge action, it is not clear from this analysis if the FNN gains high accuracy for other lattice simulations, for example, at nonzero temperature, with different lattice gauge action, and QCD with dynamical fermions. However, the results of other lattice simulations suggest that the qualitative behavior of $Q(t)$ is similar to Figs. 1 and 2 [7, 12, 14] even if the setting of the simulation is changed. It thus is naïvely expected that our method can be used successfully even for different lattice simulations, although in this case the FNN has to be trained using the data obtained by the specific simulation. Although in Sec. 6.2 we found that the input flow times $t/a^2 = (0.3, 0.25, 0.2)$ are an optimal choice for the case of SU(3) gauge theory with the Wilson gauge action, the optimal set of input flow times will also be different for different simulations.

7 Learning topological charge density $q_t(x)$

In this section we employ a CNN and train it to analyze the four-dimensional field $q_t(x)$. Motivation for this analysis is the search for characteristic features responsible for the topology in the four-dimensional space by ML. As the CNN has been applied to image recognition quite successfully [28, 31–33], it is expected that the features in four-dimensional space can also be captured by this network, and an improvement of the accuracy compared with the previous section would be observed. In particular, if the quantum gauge configurations have local structures like instantons [1], such structures would be recognized by the CNN and used for an efficient prediction of \mathcal{Q} .

7.1 Input data

Let us first discuss the choice of input data for the CNN. The gauge configurations on the lattice are described by the link variables $U_\mu(x)$, which are elements of the group $SU(3)$. The most fundamental choice for the input data is the link variables. However, as $U_\mu(x)$ is described by 72 real variables per lattice site, reduction of the data size is desirable for efficient training. Moreover, because physical observables are given only by gauge-invariant combinations of $U_\mu(x)$, the CNN must learn the concept of gauge invariance, and accordingly $SU(3)$ matrix algebra, so that it can make a successful prediction of \mathcal{Q} from $U_\mu(x)$. These concepts, however, would be too complicated for simple CNN models.

In the present study, for these reasons we use the topological charge density $q_t(x)$ as the input to the CNN. $q_t(x)$ is gauge invariant, and the degrees of freedom per lattice site is one. To suppress the size of the input data further, we reduce the lattice volume to 8^4 from 16^4 and 24^4 by average pooling as preprocessing assuming that the typical spatial size of the features in the four-dimensional space is large enough and they are not spoiled by this pooling procedure. In addition to the analysis of $q_t(x)$ at a single t value, we prepare a combined data set of $q_t(x)$ with several values of t and analyze it as multi-channel data with the CNN.

7.2 Designing CNN

In this section, we use a CNN with convolutional layers that deal with four-dimensional data. In Table 9, we show the structure of the CNN model, where d denotes the dimension of the spacetime and is set to $d = 4$ throughout this section. The model has three convolutional layers with filter size 3^4 and five output channels. In the convolutional layers, we use periodic padding for all directions to respect the periodic boundary conditions of the gauge configuration. N_{ch} denotes the number of channels of input data per lattice site; $N_{\text{ch}} = 1$

layer	filter size	output size	activation
input	-	$8^d \times N_{\text{ch}}$	-
convolution	3^d	$8^d \times 5$	logistic
convolution	3^d	$8^d \times 5$	logistic
convolution	3^d	$8^d \times 5$	logistic
global average pooling	8^d	1×5	-
full connect	-	5	logistic
full connect	-	1	-

Table 9 Design of the CNN for the analysis of the multi-dimensional data. The dimension d of the input data is 4 in Sec. 7. In Sec. 8, we analyze the data with $d = 1, 2, 3$ obtained by the dimensional reduction.

when $q_t(x)$ at a single t is fed into the CNN. We also perform multi-channel analysis by feeding $q_t(x)$ at N_{ch} flow times.

Lattice gauge theory has translational symmetry, and a shift of the spatial coordinates toward any direction does not change the value of \mathcal{Q} . To ensure that the CNN automatically respects this property, we insert a global average pooling (GAP) layer [30] after the convolutional layers. The GAP layer takes the average with respect to the spatial coordinates for each channel. The output of the GAP layer is then processed by two fully-connected layers before the final output. The logistic activation function is used for the convolutional and fully-connected layers.

The training of the CNN in this section has been mainly carried out on Google Colaboratory [67]. We use 12,000 data for the training, 2,000 data for the validation, and 6,000 data for the test, respectively. The batchsize for the minibatch training is 200. We repeat the parameter tuning for 500 epochs. Other settings of the training are the same as the previous section.

Besides the CNN model in Table 9, we have tested various variations of the model. For example, we tested the ReLU activation function in place of the logistic one. The use of the fully-connected layer in place of the GAP layer and convolutional layers with the 5^4 filter size is also tried. The number of output channels of the convolutional layers was varied up to 20. We, however, found that these variations do not improve the accuracy at all, while they typically increase the numerical cost for the training. The CNN in Table 9 is a simple but efficient choice among all these variations.

$$\beta = 6.2$$

N_{ch}	input t/a^2	P	$R_{\mathcal{Q}}$									
			-4	-3	-2	-1	0	1	2	3	4	
1	0	0.371	0	0	0	0	1.000	0	0	0	0	
1	0.1	0.401	0	0	0.002	0.255	0.702	0.341	0.008	0	0	
1	0.2	0.552	0	0.043	0.240	0.495	0.687	0.597	0.336	0.111	0	
1	0.3	0.776	0	0.391	0.687	0.760	0.821	0.794	0.740	0.569	0	
3	0.3,0.2,0.1	0.942	0.200	0.913	0.944	0.950	0.944	0.939	0.937	0.889	0.571	

$$\beta = 6.5$$

N_{ch}	input t/a^2	P	$R_{\mathcal{Q}}$									
			-4	-3	-2	-1	0	1	2	3	4	
1	0	0.388	0	0	0	0	1.000	0	0	0	0	
1	0.1	0.396	0	0	0	0.086	0.889	0.129	0	0	0	
1	0.2	0.479	0	0	0.108	0.445	0.641	0.459	0.150	0	0	
1	0.3	0.698	0	0.170	0.585	0.730	0.727	0.701	0.624	0.395	0.071	
3	0.3,0.2,0.1	0.953	0	0.830	0.951	0.956	0.952	0.962	0.968	0.953	0.286	

Table 10 Accuracy P and the recalls of individual topological sectors $R_{\mathcal{Q}}$ obtained by the analysis of the topological charge density in the four-dimensional space by the CNN. The input data has N_{ch} channels.

7.3 Results

In Table 10, we show the performance of the trained CNN with various inputs. Left two columns show N_{ch} and the flow time(s) used for the input. On the upper four rows, the results with $N_{\text{ch}} = 1$ with the input data at $t/a^2 = 0, 0.1, 0.2,$ and 0.3 are shown. The last row shows the result of the multi-channel analysis with $N_{\text{ch}} = 3$ where $q_t(x)$ at $t/a^2 = (0.3, 0.2, 0.1)$ are used. The third column shows the accuracy P of the trained CNN obtained for each input. In the table, we also show the recalls of individual topological sectors $R_{\mathcal{Q}}$ defined in Eq. (6).

The top row of Table 10 shows P and $R_{\mathcal{Q}}$ obtained by the analysis of the topological charge density of the original gauge configuration without the gradient flow. Although we obtain a nonzero P , the recall of each \mathcal{Q} shows that in this case the CNN is trained to answer $\mathcal{Q} = 0$ for almost all configurations. This means that the CNN fails in obtaining any features responsible for the determination of \mathcal{Q} .

Next, the results with $N_{\text{ch}} = 1$ but nonzero t/a^2 show that P becomes larger with increasing t/a^2 . From R_Q one also finds that the output of the CNN scatters on different topological sectors. However, by comparing P with that of the benchmark model P_{imp} in Table 3 with the same t/a^2 , one finds that P and P_{imp} are almost the same. This result suggests that the CNN is trained to answer Q_{imp} and no further information is obtained from the analysis of the four-dimensional data of $q_t(x)$.

Finally, from the multi-channel analysis with the input flow times $t/a^2 = (0.3, 0.2, 0.1)$, one finds that the accuracy P is significantly enhanced from the case with $N_{\text{ch}} = 1$ and exceeds 94% for each β . However, this accuracy is the same within the error as that obtained by the FNN in Sec. 6 with $t/a^2 = (0.3, 0.2, 0.1)$ shown in Table 5. This result implies that the CNN is trained to obtain $Q(t)$ for each t and then predicts the answer from them with a similar procedure as the FNN in Sec. 6.

From these results, it is conjectured that our analyses of four-dimensional data by CNN failed in finding structures in the four-dimensional space responsible for the determination of Q . The numerical cost for the training of the CNN in this section is a few orders larger than in Sec. 6, although a clear improvement of the accuracy is not observed. Therefore, for practical purposes the analysis in the previous section with the FNN is superior. We also note that this negative result on the analysis of four-dimensional data would be improved by changing the design of the CNN. For example, as the down-sampling of the data by the average pooling would smear out small features, direct analysis of the original data without the average pooling would modify the result. We leave this analysis for future study.

8 Dimensional reduction

In the previous two sections we discussed the analysis of the four-dimensional topological charge density $q_t(x)$ and its four-dimensional integral $Q(t)$ by ML. The spatial dimensions of these input data are $d = 4$ and 0, respectively. In this section, we analyze data with dimensions $d = 1-3$ obtained by dimensional reduction by the CNN.

We consider the integral of the topological charge density with respect to some coordinates

$$\tilde{q}_t^{(3)}(x_1, x_2, x_3) = \int dx_4 q_t(x_1, x_2, x_3, x_4), \quad (11)$$

$$\tilde{q}_t^{(2)}(x_1, x_2) = \int dx_4 dx_3 q_t(x_1, x_2, x_3, x_4), \quad (12)$$

$$\tilde{q}_t^{(1)}(x_1) = \int dx_4 dx_3 dx_2 q_t(x_1, x_2, x_3, x_4), \quad (13)$$

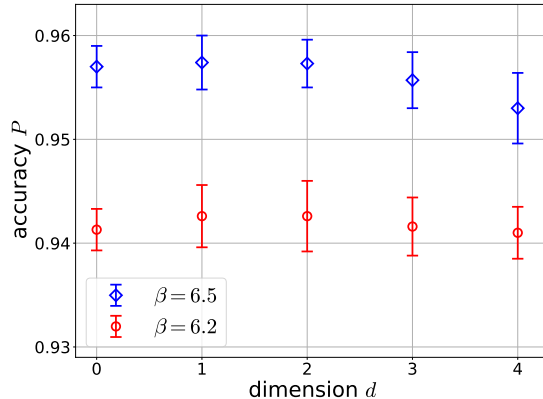


Fig. 7 Dependence of the accuracy P on the spacetime dimension d after the dimensional reduction. The values at $d = 0$ and 4 corresponds to the results in Secs. 6 and 7, respectively.

with $q_t(x) = q_t(x_0, x_1, x_2, x_3)$. Here, $\tilde{q}_t^{(d)}$ is the d -dimensional field analyzed by the CNN. The structure of the CNN is the same as in the previous section (see Table 9) except for the value of d . The procedure of the supervised learning is also the same. We analyze the multi-channel data with $N_{\text{ch}} = 3$ and $t/a^2 = (0.3, 0.2, 0.1)$.

In Fig. 7, we show the accuracy obtained by the analysis of the d -dimensional data $\tilde{q}_t^{(d)}$ by CNN. The data points at $d = 0$ show the result obtained by the analysis of $Q(t)$ by FNN in Sec. 6 with $t/a^2 = (0.3, 0.2, 0.1)$ given in Table 5. From the figure, one finds that the accuracy does not have a statistically significant d dependence, although the results at $d = 1$ and 2 would be slightly better than $d = 0$. This result supports our conjecture in the previous section that the CNN fails in finding characteristic features in the multi-dimensional data.

9 Discussion

In the present study, we have investigated the application of the machine learning techniques to the classification of the topological sector of gauge configurations in SU(3) Yang-Mills theory. The Wilson gauge action has been used for generating gauge configurations. The topological charge density $q_t(x)$ at zero and nonzero flow times t is used as input to the neural networks (NN) with and without dimensional reduction.

We found that the prediction of the topological charge \mathcal{Q} can be made most efficiently when $Q(t)$ at small flow times is used as the input of the NN. In particular, we found that the value of \mathcal{Q} defined at a large flow time can be predicted with high accuracy only with $Q(t)$

at $t/a^2 \leq 0.3$; at $\beta = 6.5$, the accuracy exceeds 99%. This result suggests that the numerical cost of solving the gradient flow toward large flow times would be omitted in the analysis of \mathcal{Q} with the aid of ML. It will be an interesting future study to pursue this possibility further by additional analyses.

Because the prediction of the NN does not have 100% accuracy, the analysis of \mathcal{Q} by NN gives rise to uncontrollable systematic uncertainties. However, our analyses indicate that the accuracy is improved as the continuum limit is approached. Moreover, as discussed in Sec. 6, the imperfect accuracy would to a large extent come from intrinsic uncertainty of the topological sectors on the lattice with finite a . It thus is expected that the analysis of \mathcal{Q} becomes more accurate as the lattice spacing becomes finer. As the 99% accuracy is already attained at $\beta = 6.5$ ($a \simeq 0.044$ fm), the analysis with the ML will be used safely for $\beta \gtrsim 6.5$.

All numerical analyses in this study have been carried out in SU(3) Yang-Mills theory with the Wilson gauge action. While the dependence on the lattice spacing, a , has been studied, the lattice volume in physical units is fixed. It thus is not clear from the present study if ML can be successfully applied to lattice simulations with different settings, such as QCD with dynamical fermions, different lattice gauge action and different lattice volumes. As discussed in Sec. 6.6, however, it is notable that the behaviors of $Q(t)$ obtained by different lattice simulations are similar to one another. It thus is naïvely expected that our method is applicable even for different lattice simulations, although this conjecture has to be checked explicitly on each setting.

We found that the analysis of the multi-dimensional field $q_t(x)$ by CNN can gain high accuracy. However, an improvement in accuracy compared with the analysis of $Q(t)$ by FNN was not observed using the CNN employed in Sec. 7 and 8. Moreover, in Sec. 8 it was found that the accuracy does not have a statistically significant dependence on the dimension of the input data. A plausible interpretation of this result is that the CNN employed in the present study fails in capturing useful structures in four-dimensional space relevant for the determination of \mathcal{Q} . It will be an interesting future work to pursue the recognition of structures in four-dimensional space using ML. One straightforward extension in this direction is analysis with a CNN having a more complex structure. In particular, analysis without preprocessing by average pooling will improve the performance if this preprocessing smears out the small features in the multi-dimensional space. Another interesting direction is analysis of gauge configurations at high temperatures where the dilute instanton-gas picture is applicable. As the topological charge should be carried by well-separated local objects at such temperatures, the search for the multi-dimensional space by CNN would be easier than the vacuum configurations. It is also interesting to analyze $q_t(x)$ at a large flow time after

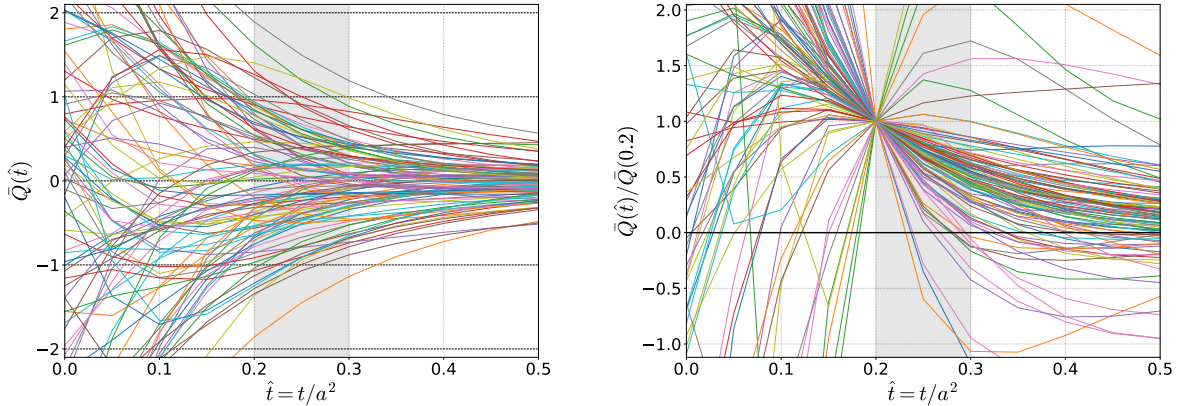


Fig. A1 Closer look at the behavior of $Q(t)$ at $\hat{t} = t/a^2 \leq 0.5$.

subtracting the average, because the NN can no longer make use of the information on $Q(t)$ by such preprocessing. We leave these analyses for future research.

The authors thank A. Tomiya for many useful discussions. They also thank H. Fukaya and K. Hashimoto. The lattice simulations of this study are in part carried out on OCTOPUS at the Cybermedia Center, Osaka University and Reedbush-U at Information Technology Center, The University of Tokyo. The NN are constructed on the Chainer framework. The supervised learning of the NN in Secs. 7 and 8 is in part carried out on Google Colaboratory. This work was supported by JSPS KAKENHI Grant Numbers 17K05442 and 19H05598.

A Behavior of $Q(t)$

In this appendix, we take a closer look at the behavior of $Q(t)$ at small t . In Fig. A1, we show the t dependence of $Q(t)$ on 100 gauge configurations at $\beta = 6.5$ in two different ways. In the upper panel we show

$$\bar{Q}(\hat{t}) = Q(\hat{t}a^2) - \mathcal{Q}, \quad (\text{A1})$$

with $\hat{t} = t/a^2$, while the lower panel shows

$$\frac{\bar{Q}(\hat{t})}{\bar{Q}(0.2)}. \quad (\text{A2})$$

Equation (A2) becomes unity at $\hat{t} = 0.2$.

In Sec. 6 it is shown that the trained NN can estimate the value of \mathcal{Q} from the behavior of $Q(t)$ at $0.2 \leq \hat{t} \leq 0.3$ with 99% accuracy for $\beta = 6.5$. This range of \hat{t} is highlighted by the gray

band in Fig. A1. From the upper panel, one sees that $\bar{Q}(\hat{t})$ approaches zero monotonically on almost all configurations. However, the panel shows that some lines deviate from this trend. As a result, it seems difficult to predict the value of Q with 99% accuracy (Q has to be predicted correctly on 99 lines among 100 in the panel) by a simple function or the human eye from the behavior at $0.2 \leq \hat{t} \leq 0.3$, although 95% accuracy is not difficult to attain. A similar observation is also obtained from the lower panel. It thus is indicated that the 99% accuracy obtained by the NN in Sec. 4 is not a trivial result.

References

- [1] Steven Weinberg, *The quantum theory of fields. Vol. 2: Modern applications*, (Cambridge University Press, 2013).
- [2] R. D. Peccei and Helen R. Quinn, Phys. Rev. Lett., **38**, 1440–1443 (Jun 1977).
- [3] John Preskill, Mark B. Wise, and Frank Wilczek, Phys. Lett. B, **120**(1), 127 – 132 (1983).
- [4] L.F. Abbott and P. Sikivie, Phys. Lett. B, **120**(1), 133 – 136 (1983).
- [5] Evan Berkowitz, Michael I. Buchoff, and Enrico Rinaldi, Phys. Rev., **D92**(3), 034507 (2015), arXiv:1505.07455.
- [6] Ryuichiro Kitano and Norikazu Yamada, JHEP, **10**, 136 (2015), arXiv:1506.00370.
- [7] Marco Cè, Cristian Consonni, Georg P. Engel, and Leonardo Giusti, Phys. Rev., **D92**(7), 074502 (2015), arXiv:1506.06052.
- [8] Claudio Bonati, Massimo D’Elia, Marco Mariti, Guido Martinelli, Michele Mesiti, Francesco Negro, Francesco Sanfilippo, and Giovanni Villadoro, JHEP, **03**, 155 (2016), arXiv:1512.06746.
- [9] Peter Petreczky, Hans-Peter Schadler, and Sayantan Sharma, Phys. Lett., **B762**, 498–505 (2016), arXiv:1606.03145.
- [10] J. Frison, R. Kitano, H. Matsufuru, S. Mori, and N. Yamada, JHEP, **09**, 021 (2016), arXiv:1606.07175.
- [11] Sz. Borsanyi et al., Nature, **539**(7627), 69–71 (2016), arXiv:1606.07494.
- [12] Yusuke Taniguchi, Kazuyuki Kanaya, Hiroshi Suzuki, and Takashi Umeda, Phys. Rev., **D95**(5), 054502 (2017), arXiv:1611.02411.
- [13] S. Aoki, G. Cossu, H. Fukaya, S. Hashimoto, and T. Kaneko, PTEP, **2018**(4), 043B07 (2018), arXiv:1705.10906.
- [14] Constantia Alexandrou, Andreas Athenodorou, Krzysztof Cichy, Arthur Dromard, Elena Garcia-Ramos, Karl Jansen, Urs Wenger, and Falk Zimmermann, arXiv:1708.00696 (2017), arXiv:1708.00696.
- [15] Florian Burger, Ernst-Michael Ilgenfritz, Maria Paola Lombardo, and Anton Trunin, Phys. Rev., **D98**(9), 094501 (2018), arXiv:1805.06001.
- [16] Peter Thomas Jahn, Guy D. Moore, and Daniel Robaina, Phys. Rev., **D98**(5), 054512 (2018), arXiv:1806.01162.
- [17] Claudio Bonati, Massimo D’Elia, Guido Martinelli, Francesco Negro, Francesco Sanfilippo, and Antonino Todaro, JHEP, **11**, 170 (2018), arXiv:1807.07954.
- [18] Leonardo Giusti and Martin Lüscher, Eur. Phys. J., **C79**(3), 207 (2019), arXiv:1812.02062.
- [19] M. Luscher, Commun. Math. Phys., **85**, 39 (1982).
- [20] M. F. Atiyah and I. M. Singer, Annals of Math., **93**(1), 139–149 (1971).
- [21] Y. Iwasaki and T. Yoshie, Phys. Lett., **131B**, 159–164 (1983).
- [22] M. Teper, Phys. Lett., **162B**, 357–362 (1985).
- [23] Luigi Del Debbio, Haralambos Panagopoulos, and Ettore Vicari, JHEP, **08**, 044 (2002), hep-th/0204125.
- [24] Sinya Aoki, Hidenori Fukaya, Shoji Hashimoto, and Tetsuya Onogi, Phys. Rev., **D76**, 054508 (2007), arXiv:0707.0396.
- [25] Stefan Schaefer, Rainer Sommer, and Francesco Virotta, Nucl. Phys. B, **845**, 93–119 (2011), arXiv:1009.5228.
- [26] Martin Luscher and Stefan Schaefer, JHEP, **07**, 036 (2011), arXiv:1105.4749.
- [27] Y. Lecun, L. Bottou, Y. Bengio, and P. Haffner, Proc. IEEE, **86**(11), 2278–2324 (Nov 1998).
- [28] Alex Krizhevsky, Ilya Sutskever, and Geoffrey E. Hinton, Imagenet classification with deep convolutional neural networks, In *Proceedings of the 25th International Conference on Neural Information Processing Systems - Volume 1*, NIPS’12, pages 1097–1105, USA (2012). Curran Associates Inc.
- [29] Quoc Le, Marc’Aurelio Ranzato, Rajat Monga, Matthieu Devin, Kai Chen, Greg Corrado, Jeff Dean, and Andrew Ng, Building high-level features using large scale unsupervised learning, In *Proceedings of the 29th International Conference on Machine Learning (ICML-12)*, ICML ’12, pages 81–88, New York, NY, USA (July 2012). Omnipress.
- [30] Min Lin, Qiang Chen, and Shuicheng Yan, arXiv:1312.4400 (Dec 2013), arXiv:1312.4400.
- [31] Christian Szegedy, Wei Liu, Yangqing Jia, Pierre Sermanet, Scott Reed, Dragomir Anguelov, Dumitru Erhan,

- Vincent Vanhoucke, and Andrew Rabinovich, Going deeper with convolutions, In *CVPR* (June 2015).
- [32] K. Simonyan and A. Zisserman, Very deep convolutional networks for large-scale image recognition, In *International Conference on Learning Representations* (2015).
- [33] Kaiming He, Xiangyu Zhang, Shaoqing Ren, and Jian Sun, Deep residual learning for image recognition, In *CVPR* (June 2016).
- [34] Ross Girshick, Jeff Donahue, Trevor Darrell, and Jitendra Malik, Rich feature hierarchies for accurate object detection and semantic segmentation, In *CVPR* (June 2014).
- [35] Ross Girshick, Fast r-cnn, In *ICCV* (December 2015).
- [36] Wei Liu, Dragomir Anguelov, Dumitru Erhan, Christian Szegedy, Scott Reed, Cheng-Yang Fu, and Alexander C. Berg, SSD: Single shot multibox detector, In *ECCV* (June 2016).
- [37] Shaoqing Ren, Kaiming He, Ross Girshick, and Jian Sun, In *Advances in Neural Information Processing Systems 28*, page 91. Curran Associates, Inc. (2015).
- [38] Joseph Redmon, Santosh Divvala, Ross Girshick, and Ali Farhadi, You only look once: Unified, real-time object detection, In *CVPR* (June 2016).
- [39] Tomas Mikolov, Ilya Sutskever, Kai Chen, Greg S Corrado, and Jeff Dean, In *Advances in Neural Information Processing Systems 26*, page 3111 (2013).
- [40] Ashish Vaswani, Noam Shazeer, Niki Parmar, Jakob Uszkoreit, Llion Jones, Aidan N Gomez, Łukasz Kaiser, and Illia Polosukhin, In *Advances in Neural Information Processing Systems 30*, page 5998 (2017).
- [41] Jacob Devlin, Ming-Wei Chang, Kenton Lee, and Kristina Toutanova, arXiv:1810.04805 (2018).
- [42] Aaron van den Oord, Sander Dieleman, Heiga Zen, Karen Simonyan, Oriol Vinyals, Alexander Graves, Nal Kalchbrenner, Andrew Senior, and Koray Kavukcuoglu, Wavenet: A generative model for raw audio, In *arxiv:1609.03499* (2016).
- [43] Volodymyr Mnih, Koray Kavukcuoglu, David Silver, Andrei A. Rusu, Joel Veness, Marc G. Bellemare, Alex Graves, Martin Riedmiller, Andreas K. Fidjeland, Georg Ostrovski, Stig Petersen, Charles Beattie, Amir Sadik, Ioannis Antonoglou, Helen King, Dhharshan Kumaran, Daan Wierstra, Shane Legg, and Demis Hassabis, *Nature*, **518**(7540), 529–533 (February 2015).
- [44] David Silver, Julian Schrittwieser, Karen Simonyan, Ioannis Antonoglou, Aja Huang, Arthur Guez, Thomas Hubert, Lucas Baker, Matthew Lai, Adrian Bolton, Yutian Chen, Timothy Lillicrap, Fan Hui, Laurent Sifre, George van den Driessche, Thore Graepel, and Demis Hassabis, *Nature*, **550**, 354– (October 2017).
- [45] I. E. Lagaris, A. Likas, and D. I. Fotiadis, *IEEE Trans. Neural Networks*, **9**(5), 987–1000 (Sep. 1998).
- [46] Pierre Baldi, Peter Sadowski, and Daniel Whiteson, *Nature Commun.*, **5**, 4308 (2014), arXiv:1402.4735.
- [47] Luke de Oliveira, Michael Kagan, Lester Mackey, Benjamin Nachman, and Ariel Schwartzman, *JHEP*, **07**, 069 (2016), arXiv:1511.05190.
- [48] Tomoki Ohtsuki and Tomi Ohtsuki, *J. Phys. Soc. Jap.*, **85**(12), 123706 (2016), <https://doi.org/10.7566/JPSJ.85.123706>.
- [49] James Barnard, Edmund Noel Dawe, Matthew J. Dolan, and Nina Rajcic, *Phys. Rev.*, **D95**(1), 014018 (2017), arXiv:1609.00607.
- [50] Akinori Tanaka and Akio Tomiya, *J. Phys. Soc. Jap.*, **86**(6), 063001 (2017), arXiv:1609.09087.
- [51] Juan Carrasquilla and Roger G. Melko, *Nature Phys.*, **13**, 431 EP – (Feb 2017).
- [52] Sebastian Johann Wetzal and Manuel Scherzer, *Phys. Rev. B*, **96**(18), 184410 (2017), arXiv:1705.05582.
- [53] Yuto Mori, Kouji Kashiwa, and Akira Ohnishi, *Phys. Rev.*, **D96**(11), 111501 (2017), arXiv:1705.05605.
- [54] Maziar Raissi, Paris Perdikaris, and George Em Karniadakis, arXiv:1711.10561 (2017).
- [55] Hengfeng Huang, Bowen Xiao, Huixin Xiong, Zeming Wu, Yadong Mu, and Huichao Song, arXiv:1081.03334 (2018), arXiv:1801.03334.
- [56] Phiala E. Shanahan, Daniel Trewartha, and William Detmold, *Phys. Rev.*, **D97**(9), 094506 (2018), arXiv:1801.05784.
- [57] Koji Hashimoto, Sotaro Sugishita, Akinori Tanaka, and Akio Tomiya, *Phys. Rev.*, **D98**(4), 046019 (2018), arXiv:1802.08313.
- [58] Kouji Kashiwa, Yuta Kikuchi, and Akio Tomiya, *PTEP*, **2019**(8), 083A04 (2019), arXiv:1812.01522.
- [59] Jan Steinheimer, Longgang Pang, Kai Zhou, Volker Koch, Jørgen Randrup, and Horst Stoecker, arXiv:1906.06562 (2019), arXiv:1906.06562.
- [60] Kenji Fukushima, Shotaro Shiba Funai, and Hideaki Iida, arXiv:1908.00281 (2019), arXiv:1908.00281.
- [61] R. Narayanan and H. Neuberger, *JHEP*, **03**, 064 (2006), arXiv:hep-th/0601210.
- [62] Martin Lüscher, *JHEP*, **08**, 071, [Erratum: *JHEP*03,092(2014)] (2010), arXiv:1006.4518.
- [63] Martin Luscher and Peter Weisz, *JHEP*, **02**, 051 (2011), arXiv:1101.0963.
- [64] Masakiyo Kitazawa, Takumi Iritani, Masayuki Asakawa, Tetsuo Hatsuda, and Hiroshi Suzuki, *Phys. Rev.*, **D94**(11), 114512 (2016), arXiv:1610.07810.
- [65] Diederik P. Kingma and Jimmy Ba, arXiv:1412.6980 (Dec 2014), arXiv:1412.6980.

[66] Chainer, <https://chainer.org/> ().

[67] Google colaboratory, <https://colab.research.google.com/> ().